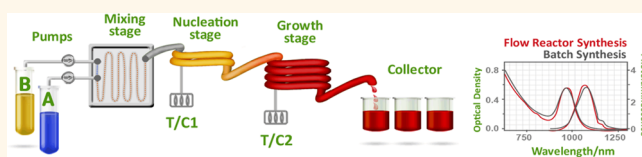


Automated Synthesis of Photovoltaic-Quality Colloidal Quantum Dots Using Separate Nucleation and Growth Stages

Jun Pan,^{†,||} Ala'a O. El-Ballouli,^{†,||} Lisa Rollny,^{†,||} Oleksandr Voznyy,[‡] Victor M. Burlakov,[§] Alain Goriely,[§] Edward H. Sargent,^{*,*} and Osman M. Bakr^{†,*}

[†]Division of Physical Sciences and Engineering, Solar and Photovoltaics Engineering Center, King Abdullah University of Science and Technology (KAUST), Thuwal 23955-6900, Saudi Arabia, [‡]Department of Electrical and Computer Engineering, University of Toronto, 10 King's College Road, Toronto, Ontario M5S 3G4, Canada, and [§]Mathematical Institute, University of Oxford, Woodstock Road, Oxford OX2 6GG, U.K. ^{||}These authors contributed equally.

ABSTRACT As colloidal quantum dot (CQD) optoelectronic devices continue to improve, interest grows in the scaled-up and automated synthesis of high-quality materials. Unfortunately, all reports of record-performance CQD photovoltaics have been based on small-scale batch syntheses. Here we report a strategy for flow reactor synthesis of PbS CQDs and prove that it leads to solar cells having performance similar to that of comparable batch-synthesized nanoparticles. Specifically, we find that, only when using a dual-temperature-stage flow reactor synthesis reported herein, are the CQDs of sufficient quality to achieve high performance. We use a kinetic model to explain and optimize the nucleation and growth processes in the reactor. Compared to conventional single-stage flow-synthesized CQDs, we achieve superior quality nanocrystals *via* the optimized dual-stage reactor, with high photoluminescence quantum yield (50%) and narrow full width-half-maximum. The dual-stage flow reactor approach, with its versatility and rapid screening of multiple parameters, combined with its efficient materials utilization, offers an attractive path to automated synthesis of CQDs for photovoltaics and, more broadly, active optoelectronics.



KEYWORDS: PbS · flow reactor · synthesis · colloidal quantum dots · photovoltaics · scalable manufacturing

Colloidal quantum dots (CQDs) are versatile materials of interest in many fields in view of their programmable optoelectronic properties.^{1,2} PbS CQDs are of particular interest in solar photovoltaic applications, in which the semiconductor's large Bohr exciton radius enables quantum-size-effect tuning over the broad solar spectrum, including the infrared portion.² Compared to other third-generation photovoltaic materials such as CIGS^{3,4} and CZTS,^{5,6} CQDs offer avenues to tandem and multijunction solar cells from a single material *via* size-effect bandgap tunability. Moreover, their processing from the solution phase should in principle allow rapid, large-scale manufacturing and ready integration with flexible substrates, facilitating roll-to-roll processing.

Herein we identify, and then address, one key impediment that currently prevents CQDs from fulfilling their tremendous promise. All prior reports of the best-performing CQD photovoltaics^{7–9} have relied on a manual batch synthesis. In this work, we

develop an automated, scalable, in-line synthesis methodology. We show that, only by incorporating an innovative two-stage reactor system, can we achieve the monodispersity and surface quality required to reach the best previously reported CQD photovoltaic performance.

The traditional CQD batch synthesis relies on elemental precursor solutions; organic surfactants that will act as ligands; and a dispersing solvent.^{10,11} In the standard hot-injection method, a solution containing one precursor (precursor A in Figure 1a) is heated to a chosen temperature, and a second precursor (precursor B) is injected into this solution. Sudden nucleation of CQD seeds occurs and is followed by particle growth, yielding a monodisperse distribution of CQDs.¹² Scaling up such syntheses in a batch setup is limited by the difficulties associated with quenching the reaction over a small time interval inside a large reactor, as well as the increase of spatial chemical gradients associated with larger reactor volumes.¹³

* Address correspondence to osman.bakr@kaust.edu.sa, ted.sargent@utoronto.ca.

Received for review August 22, 2013 and accepted October 16, 2013.

Published online October 16, 2013 10.1021/nn404397d

© 2013 American Chemical Society

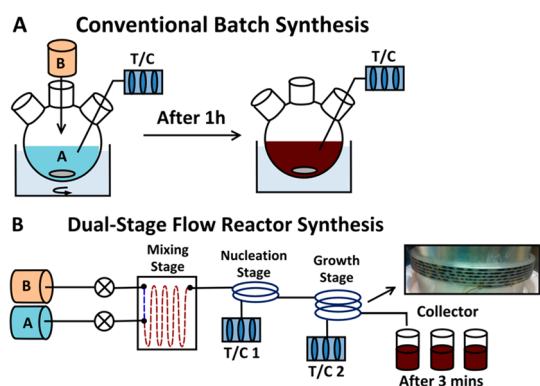


Figure 1. Schematic of (a) a conventional batch synthesis setup and (b) a dual-stage continuous flow reactor setup with precursor A (Pb-oleate, ODE) and precursor B (TMS in ODE).

In the past decade, continuous flow synthesis has emerged as a compelling technology enabling large-scale production while offering several advantages including improved control of heat and mass transfer, precise cooling rates, and reproducibility.^{14–16} Additionally, the flow regime allows rapid screening of parameters, automation, and low reagent consumption during optimization.¹⁶ In flow synthesis, the use of a narrow channel diameter decreases the dispersion in the velocity of the solution, potentially enabling a higher degree of monodispersity. Since the first flow synthesis of nanocrystals in 2002,¹⁷ a variety of nanomaterials have been synthesized using flow reactors,^{18,19} including a wide range of metal,^{20–25} metal oxide,^{26–31} and even metal/metal oxide core-shell nanoparticles.³² Even though the synthesis of colloidal quantum dots (CQDs), such as CdS,^{33,34} CdSe,^{13–16,33,35–37} InP,³⁸ and SnTe,³⁹ *via* flow reactor synthesis is becoming increasingly popular, achieving a high-quality product remains a challenge. Prior efforts have sought to narrow the particle size distribution *via* segmented flow instead of the traditional laminar flow.^{14,27,34,35} By segmenting the flow of the reacting phase with an immiscible inert liquid (i.e., liquid–liquid segmentation), the reagent dispersion becomes confined to the volume of the isolated droplets rather than dispersing along the entire length of the channel.^{16,40} Accordingly, the flow of droplets provides high mixing efficiency, which is essential in particle size control. Distributed temperature zones within a capillary microreactor have been applied in previous work to synthesize narrower size-distribution CdSe CQDs.¹³ Inspired by this work, we use a dual-temperature-stage coil-reactor system to realize high quality PbS quantum dots by controlling the nucleation and growth process guided by theory and modeling.

RESULTS AND DISCUSSION

The flow reactor system created for the present work is depicted schematically in Figure 1b. Precursor

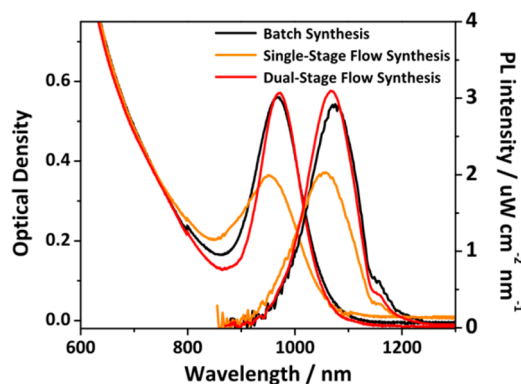


Figure 2. Absorbance and PLQE of PbS CQDs synthesized with a single-stage flow approach compared to batch synthesis and dual-stage flow setup.

solutions are prepared in the same manner as in batch synthesis, only deviating by the addition of an inert, immiscible fluid (Fluorinert FC-70) that aids in maintaining clean reaction channels and keeping a consistent reaction volume and flow rate. Precursor A consists of lead oxide, oleic acid (OA), and octadecene (ODE). Precursor B contains bis(trimethylsilyl) sulfide (TMS) and ODE. The two precursors are injected under N₂ overpressure through micropumps at different points into the mixing stage. The temperature of this stage is set low enough to prevent premature reaction of the compounds. The mixed reactants proceed together to the nucleation stage that is temperature-controlled by thermocouple 1. The elevated temperature causes the precursors to react and form nucleation seeds. The purification procedure is similar to the established batch synthesis, involving precipitation of the CQDs using acetone and subsequent redispersal in toluene.

We investigated absorbance and photoluminescence behavior of CQDs produced using this single-temperature stage approach. At a reaction temperature of 75 °C, the approach yielded CQDs with lower quality than their conventional batch synthesis counterpart, seen in the less defined excitonic feature (notably lower peak-to-valley ratio, Figure 2). Additionally, we found that the nanoparticles have a lower photoluminescence quantum efficiency (PLQE), as well as a broader full-width-at-half-maximum (fwhm) of the PL signal, as summarized in Table 1.

We hypothesized that much greater control over the temperature profile in time/space in the flow chamber would be required to produce high-quality CQDs. By separating the nucleation and growth processes, we aimed to increase the degree of control over these two steps. This would allow growth to occur at a lower temperature than the nucleation temperature and lead to a narrower size distribution of the CQD population.

Table 1 summarizes the synthesis conditions and key quality indicators for CQDs having a bandgap of ~1.3 eV for three cases: batch, single-stage flow, and

TABLE 1. Reaction Conditions and Optical Quality Assessment of PbS CQDs Produced by Batch Synthesis and Single-Stage and Dual-Stage Flow Synthesis with T_N Being the Injection Temperature To Start Nucleation in the Batch Synthesis and in the Nucleation Stage of a Flow Reactor, T_G Being the Temperature at Which Growth Occurs, and PLQE and FWHM of PL Signal To Verify CQD Quality

synthesis type	T_N (°C)	T_G (°C)	Abs position (nm)	PL position (nm)	PLQE (%)	fwhm (eV)
batch synth	90	slow cooling	968	1071	48.8	0.114
single-stage flow synth	—	75	951	1052	28.2	0.131
dual-stage flow synth	120	90	970	1065	50.6	0.110

dual-stage flow syntheses. CQDs made using the dual-stage flow synthesis are superior in their lower Stokes shift, higher PLQE, and a narrower PL fwhm compared to single-stage flow synthesis.

In a two-stage reactor such as the one depicted in Figure 1b, there are at least three main experimental parameters that can be varied independently: the temperature of the nucleation stage (T_N), the temperature of the growth stage (T_G), and the total residence time t_R . The interplay between those parameters affects the particle size and distribution in a nontrivial manner. We used a theoretical model of particle nucleation and growth from a one-component solution to understand qualitatively these effects and to guide the optimization of the reactor system thereby achieving high-quality monodisperse CQDs. In this simple model, we assume that the nucleation of particles takes place only in the first stage controlled by T_N , while the growth, and possibly Ostwald ripening, processes are controlled only by T_G in the second stage and are independent of the nucleation stage.

Within this framework, particle nucleation and growth is characterized by two key parameters: the critical radius, R_C and the Gibbs–Thomson concentration $n_{GT}(R, T)$.^{41–43} The former determines the smallest possible particle radius produced in the nucleation stage, while the latter determines the growth rate of particles in both stages. Under the conditions of thermal equilibrium between a given particle and the surrounding solution, we may equate chemical potentials of atoms/molecules in solution with their counterparts in a particle of radius R by

$$RT \ln \left(\frac{n}{N_0} \right) - \varepsilon_L = -\varepsilon_S + \frac{2v_m \gamma}{R} \quad (1)$$

where R is the universal gas constant, T is the absolute temperature, n is the solution concentration, N_0 is the hypothetical saturation concentration,⁴⁴ ε_L and ε_S ($\varepsilon_{L,S} > 0$ and $\varepsilon_S > \varepsilon_L$) are the absolute values of the materials energy per mole in the solution and solid state, respectively, v_m is the molar molecular volume, and γ is the surface energy per particle surface unit area. The critical radius is obtained from eq 1 for any

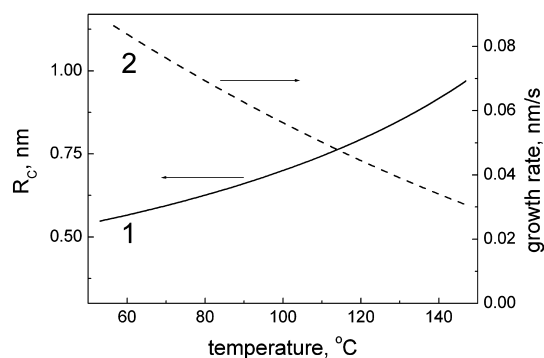


Figure 3. Temperature dependence of the critical radius R_C (solid line) and the growth rate $W(R_C \cdot (1 + \delta), T)$ (dashed line) calculated using eqs 2 and 3, respectively, for $D = 10^{-12} \text{ m}^2/\text{s}$, $K = 2 \times 10^{-5} \text{ m/s}$, $v_m = 3 \times 10^{-5} \text{ m}^3/\text{mol}$, $\Delta_1 = 55 \text{ kJ/mol}$, $\gamma = 0.2 \text{ J/m}^2$, $N_0 = 4 \cdot 10^4 \text{ mol/m}^3$, $n_{b1} = 76$, and $\delta = 0.05$.

concentration $n = n_0$ as

$$R_C = \frac{2v_m \gamma}{RT_N \ln(n_0/N_0) + \Delta_1} \quad (2)$$

with $\Delta_1 \equiv \varepsilon_S - \varepsilon_L$, while the Gibbs–Thomson concentration is derived under the condition of fixed R as $n_{GT}(R, T) = N_0 \exp[-((\Delta_1)/(k_B T)) + ((2v_m \gamma)/(R \cdot RT))]$. To understand the capabilities of the dual-stage reactor, consider the generalized classical mean-field theory of Ostwald ripening⁴⁴ in the case of supersaturation. According to the derivation in section 1 in Supporting Information, we may write the main equation for particle size growth rate $W(R, T)$ as

$$\frac{dR}{dt} = W(R, T) = \frac{N_0 \cdot v_m \cdot K \cdot D}{D + K \cdot R} \cdot \exp \left[-\frac{\Delta_1}{RT} \right] \cdot \left(n_{b1} - \exp \left[\frac{2v_m \gamma}{R \cdot R \cdot T} \right] \right) \quad (3)$$

where D is the molecular diffusion coefficient in the solution, K is the interface reaction rate, and n_{b1} is the solution concentration relative to $n_{GT}(R = \infty, T)$. According to eq 3, the size growth rate is a result of each particle absorbing an atomic flux proportional to n_{b1} and emitting an atomic flux proportional to n_{GT} , with the proportionality coefficient determined by both the atomic diffusion coefficient D and the interface reaction rate K . If $n_{b1} \gg 1$ then all nucleated particles grow but with different rates: larger particles grow faster than the smaller ones, suggesting that the absolute value of the particle size distribution (PSD) increases during this active growth stage.

Figure 3 shows a plot of $R_C(T)$ and $W((1 + \delta) \cdot R_C, T)$ during the nucleation stage of the reactor, where $\delta \ll 1$ is a constant reflecting small fluctuational growth of the nucleated particle above R_C (since $W(R_C, T) = 0$). When particles initially nucleate their radius is around R_C and they are in an unstable equilibrium with the solution: they may grow or collapse depending on whether their radius is increased or decreased due to fluctuations. Particles with supercritical sizes ($R > R_C$) continue to grow during their passage through the

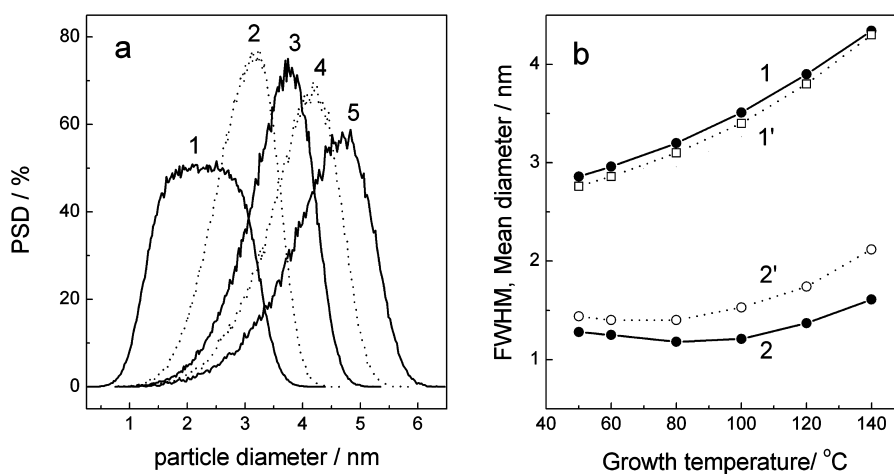


Figure 4. (a) Simulated particle size distributions (PSD): before the growth stage (1), modeled as a sum of Gaussians with an onset centered around the critical size, and after the growth stage with temperature 60 °C (2), 100 °C (3), 120 °C (4), and 140 °C (5). $T_N = 120$ °C for all curves. (b) Mean particle diameter (curves 1 and 1') and the fwhm of the PSD (curves 2 and 2') as a function of growth temperature ($T_N = 120$ °C). The results were obtained by integrating eq 3 up to the time of $t = 120$ s for an ensemble of 5×10^5 particles with n_{b1} given by eq 4. Parameter values used in our simulations of PSD and to obtain the curves 1 and 2 are $D = 5 \times 10^{-14}$ m²/s and $K = 10^{-4}$ m/s. The curves 1' and 2' have been calculated with $D = 10^{-12}$ m²/s and $K = 2 \times 10^{-5}$ m/s. All other parameters are the same as the ones in the caption of Figure 3.

nucleation stage at a rate dependent on T_N as indicated in Figure 3. Therefore, the width of the particle size distribution exiting the stage is approximately given by the size difference between particles that have nucleated at the start of the stage and those nucleated at its end. The latter have a radius close to R_C . According to Figure 3, the growth rate decreases as a function of T_N ; therefore, higher T_N values result in narrower size distributions. However, R_C and hence the nucleation barrier, increases at elevated T_N resulting in a much lower number of nucleated particles and a greater proportion of subcritical particles with $R < R_C$. Note that the subcritical particles, which are unstable in the nucleation stage, could also broaden the particle size distribution because they are quenched and become stable as soon as they exit the stage to a cooler zone (since R_C decreases with temperature). Consequently, the choice of T_N for optimal size dispersity of the product nanoparticles is a balance between those two factors.

Following a similar line of reasoning, if the residence time in the nucleation stage is relatively short the fraction of subcritical particles will be very high because it takes a while until some of them become critical or supercritical. It is thus important for the total residence time t_R to be long enough to keep the fraction of subcritical particles low yet short enough to avoid overbroadening the size distribution for supercritical particles through growth.

As the supersaturation decreases, coarsening may become important. During coarsening, bigger particles continue to grow while smaller particles dissolve, which could result in a narrower PSD, as the dissolution of many smaller particles proceeds faster than the growth of the bigger, but fewer, particles.

To understand better the impact of the coarsening process on the PSD, we simulated the evolution of an ensemble of 5×10^5 particles assuming that the active growth stage of particles has concluded (the solution is no longer supersaturated). The simulations were carried out by numerically solving eq 3 for each particle within a fixed time period; which was determined by the duration of the growth stage (see the Supporting Information for simulation details). The value of n_{b1} was determined self-consistently at every time step by equating all absorbed atomic fluxes to all emitted ones⁴⁵ (i.e., no supersaturation condition) according to the following equation:

$$n_{b1} = \left\langle \frac{R^2}{1 + R \cdot K/D} \cdot \exp \left[\frac{2v_m \gamma}{R \cdot RT} \right] \right\rangle \cdot \left\langle \frac{R^2}{1 + R \cdot K/D} \right\rangle^{-1} \quad (4)$$

Simulation results are presented in Figure 4 for two sets of D and K values. Figure 4a shows plots of the simulated particle size-distribution for $T_N = 120$ °C and different growth temperatures. For illustrative purposes, we assume that the particles enter the growth stage with a hypothetical size-distribution depicted by curve 1, which includes many subcritical particles. During the initial stages of ripening these subcritical particles quickly dissolve, transferring their mass to the supercritical ones. This transient process focuses the size distribution before reaching steady-state Ostwald ripening whereupon the distribution begins to broaden again. Since the rate of mass transfer strongly depends on temperature through the Gibbs–Thomson concentration, one may expect (for a fixed time period in the growth stage) a relatively wide initial size-distribution to narrow as a function of T_G before

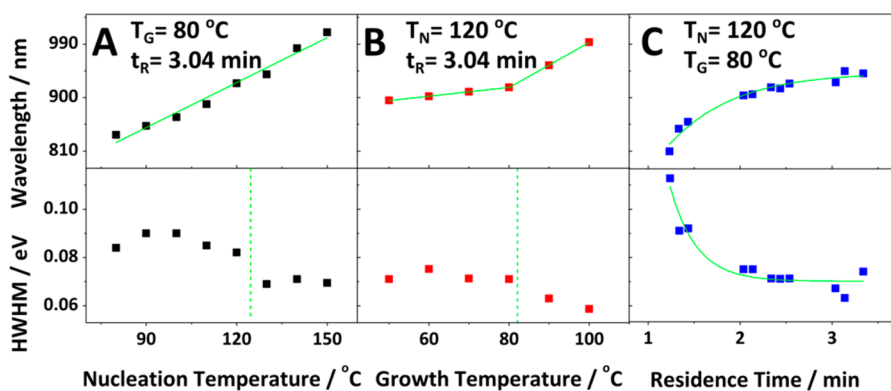


Figure 5. Absorbance and HWHM of PbS CQDs synthesized with a dual-stage apparatus while (a) varying temperature for the nucleation temperature stage, (b) varying temperature for the growth temperature stage, and (c) varying residence time.

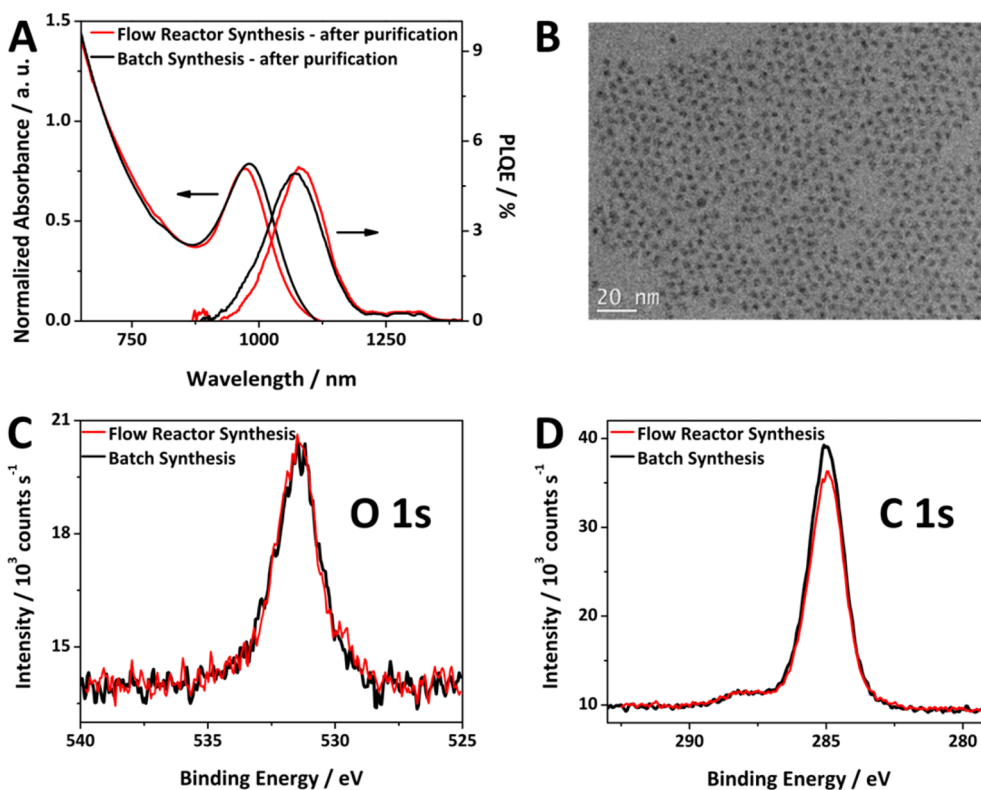


Figure 6. (a) Comparison of the absorption spectra and PLQE of traditional synthesis of quantum dots with the dual-stage flow synthesis after purification showing comparable fwhm. (b) TEM image of PbS CQD ($\lambda_{\max} \approx 950$ nm) synthesized by flow reactor. XPS comparison for the dual-stage flow synthesized dots and the traditional synthesized dots: (c) element O 1s, (d) element C 1s.

broadening again at higher temperatures due to a transition to a steady-state ripening regime^{41–45} (Figure 4b). This narrowing of the PSD depends upon the ratio KR/D . The PSD is narrower for $KR/D = 4$, (corresponding to the K and D values used in calculating curves 1 and 2 in Figure 4b) than for $KR/D = 0.02$ (curves 1' and 2'). The values of D and K are not known in our case therefore the only indication of the real KR/D ratio might come from the comparison of the calculated PSD width with the experimental one. Although both sets of D and K values produce qualitatively similar trends, the case of $KR/D = 4$ is in closer

quantitative agreement with the experimental results analyzed in our work, which suggests an intermediate ripening case between diffusion-limited and reaction-limited^{46,47} regimes.

Guided by the above theoretical arguments, we explored detailed optimization of the dual-stage approach by separately varying T_N , T_G , and t_R . The main parameters used as the indicators of the optimization quality are the half-width-at-half-maximum (HWHM) and the position of the excitonic absorption peak for each PbS CQD sample (Figure 5). Keeping t_R fixed at about 3 min, we investigated the impact of

T_N (Figure 5a) on the peak position and HWHM at constant $T_G = 80^\circ\text{C}$ and the impact of T_G at constant $T_N = 120^\circ\text{C}$. Increasing nucleation temperature shifts the CQD excitonic peak to higher wavelength, indicating larger particles. From the HWHM, we find that an optimum T_N is around 120°C , above which a sudden transition to narrower peak width occurs. To achieve the optimal single-junction solar cell bandgap of $\sim 1.3\text{ eV}$, combined with a narrow particle size distribution, we then fixed the nucleation temperature at $T_N = 120^\circ\text{C}$ in subsequent experiments. When studying the effect of growth temperature T_G (Figure 5b), we kept t_R at 3 min. For growth temperatures below 80°C a moderate increase of the absorption peak wavelength and commensurable increase in HWHM is observed. Above 80°C , the increase is much steeper and the HWHM decreases rapidly. This behavior is explained in our qualitative analysis by a broader distribution of particle growth rates (see Figure 4). Lastly, we optimized the residence time t_R at constant T_N (120°C) and T_G ranging from 80 to 90°C and found that the smallest HWHM for an excitonic peak wavelength of $\sim 950\text{ nm}$ was achieved using $\sim 3\text{ min}$.

We conducted a detailed spectroscopic and compositional analysis of optimized dual-stage flow synthesis CQDs compared to the best reported batch synthesis (Figure 6a). The HWHM of this optimized procedure is comparable to batch-synthesized dots. Following purification by precipitation and redispersion, the flow reactor CQDs remain highly monodisperse, as seen from the narrow HWHM of excitonic peak and by the high quality of the nanocrystals in TEM images (Figure 6b). A comparable amplitude of photoluminescence further confirms the quality of the CQDs. The elemental composition of the two synthesis methods was compared using X-ray photoelectron spectroscopy (XPS). Carbon and oxygen contents of the flow reactor synthesized PbS CQDs agree well with the signatures seen in XPS of batch synthesized CQDs (Figure 6c). The same agreement is observed for lead and sulfur binding energy signatures in Figure S1 (Supporting Information). Importantly, the scalability of our optimized procedure is manifested by comparing the yield to the traditional batch synthesis. A typical dual-stage flow synthesis of PbS QDs yields approximately $40\text{--}42\text{ mg/min}$ which translates to $2.4\text{--}2.5\text{ g/h}$, compared to the batch synthesis which yields around 1 g/h with two simultaneous reaction setups.

Having validated the quality of the PbS CQDs material synthesized in the dual-stage flow reactor approach, we proceeded to fabricate photovoltaic devices in the depleted heterojunction architecture,⁴⁸ in which the TiO_2 film serves as the n-type semiconductor. We measured the current–voltage characteristics (Figure 7a) in an inert nitrogen environment under 100 mW cm^{-2} simulated AM1.5G illumination and the corresponding qualitative external quantum

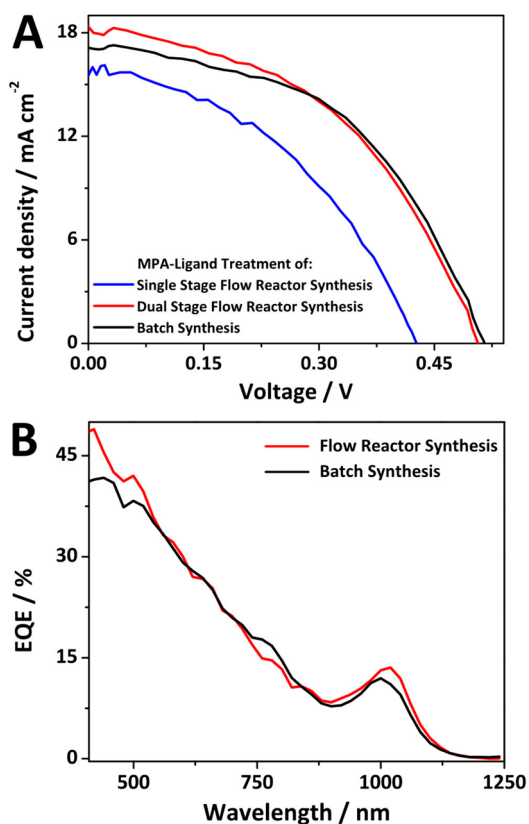


Figure 7. Photovoltaic devices made based on PbS CQD obtained from batch synthesis, single-stage flow reactor synthesis, and dual-stage flow reactor synthesis with MPA treatment to compare (a) their JV-characteristics and (b) EQE response for dual-stage flow reactor synthesis and batch synthesis.

efficiency (EQE) spectrum (Figure 7b) of PbS CQDs devices made from conventional or flow reactor methods. Devices made from the dual-stage flow reactor process are superior compared to the single-stage setup and exhibited solar power conversion efficiency (PCE) of 4.1% with an open circuit voltage of 0.53 V, a short circuit current density of 17.88 mA/cm^2 , and a fill factor of 46%; which is comparable with the batch devices. The EQE spectra of the dual-stage flow and batch devices are in good agreement with one another and demonstrate that the dots obtained from the flow reactor possess good quantum efficiency.

CONCLUSIONS

In summary, we obtained high-quality PbS CQDs with high photoluminescence quantum yield and narrow full width-half max values *via* a scalable and automated flow-synthesis methodology. As suggested by theory and confirmed by experiment, applying a dual-stage in the flow reactor is essential for the controllable synthesis of high quality CQDs. The solar cell fabricated from the flow-synthesized PbS CQDs achieves on-par performance with the batch synthesized CQDs at a power conversion efficiency of 4.1%. Future work will entail integration of improved

passivation strategies of the PbS CQD's surface, such as hybrid passivation, into a more elaborated automated synthesis, with the goal of exceeding the best published performance recently achieved with the benefits of halide passivation processes.⁷ In light of the results reported herein, it is clear that

the flow reactor approach, with its versatility and rapid screening of multiple parameters, combined with its efficient materials utilization, offers an attractive path to automated synthesis of CQDs for photovoltaics and, more broadly, active optoelectronics.

METHODS AND MATERIALS

Chemicals. Lead(II) oxide powder (PbO, 99%), oleic acid (OA, technical grade 90%), and bis(trimethylsilyl) sulfide (TMS, 95% purity) were purchased from J. T. Baker, Alpha Aesar, and Acros Organics, respectively. 1-Octadecene (ODE, technical grade 90%), acetone (ACS reagent, $\geq 99.5\%$), toluene (anhydrous, 99.8%), and octane (anhydrous, $\geq 99\%$) were purchased from Sigma-Aldrich. Fluorinert liquid (FC-70 type) was purchased from Fisher Scientific. ODE was degassed by pumping at 100 °C overnight before use, while the other chemicals were used as received without further purification.

PbS CQD Preparation. The conventional batch synthesis of oleic-acid capped PbS CQDs was based on the procedure described by Hines and Scholes using lead oleate and bis(trimethylsilyl) sulfide (TMS) as precursors.¹¹ This procedure was adapted in a continuous flow synthesis method using a commercially available continuous flow reactor, the FlowSyn Multi-X system (Uniqsis Ltd., Cambridge UK). The lead oleate precursor was prepared by dissolving lead oxide (PbO, 0.9 g) and oleic acid (OA, 3 mL) in 6 mL of 1-octadecene (ODE) and pumping the solution for 16 h at 100 °C. Then, 30 mL of ODE and 20 mL of Fluorinert FC-70⁴⁹ were added to the lead precursor solution. The mixture was transferred to bottle A and maintained at 60 °C to prevent solidification of the precursor. A stock solution of the sulfur precursor (bottle B) was prepared by mixing 360 μ L of TMS with 20 mL ODE and 20 mL FC-70 in a glovebox. Both bottles were maintained under continuous vigorous stirring (to maintain a homogeneous mixture between the different liquid phases) and nitrogen purging throughout the reaction. The flow rate was typically set within the range 1–3 mL/min. The nucleation temperature was varied in the range of 80–150 °C, while the growth temperature was set between 50 and 100 °C. After passing through the mixing and thermal stages, the product was collected in vials containing acetone to quench the reaction. The CQDs were washed several times by precipitation with acetone and redispersion in toluene. Finally, the CQDs were redispersed in octane.

Characterization. Linear optical absorption spectra were taken using a Cary UV–vis–NIR spectrometer (Varian). Glass cuvettes with a path length of 1 mm were used. For measurement purposes, the concentration of the CQD solution was adjusted to 0.4 mg/mL. PLQE measurements were performed at room temperature in air. A 640 nm diode laser with an intensity of approximately 10 W cm⁻² was used as an excitation source. A NIR spectrometer with an InGaAs array detector (Ocean Optics NIR-512, calibrated using a tungsten halogen lamp as a known source) was connected through fiber optics with an integrating sphere where the sample was positioned. The laser light is directed to enter one of the two ports of the integrating sphere. The second port is connected to an optical fiber to collect direct and indirect excitation mode spectra using the same NIR spectrometer. Low PbS CQD concentrations were used in these measurements to guarantee low reabsorption by the sample of the emitted PL signal. PLQE is calculated by taking the integrated difference between the directly excited and indirectly excited photoluminescence photon signals divided by the integrated difference between the direct-pump and indirect-pump laser photon signals. XPS was measured with a Thermo Scientific K-Alpha spectrometer to confirm material composition before and after ligand exchange. A survey measurement was taken first, followed by recording the core level spectra of Pb-4f, S-2p, O-1s, and C-1s with a pass energy of 50 eV. The binding energy was referenced to the C1s hydrocarbon line at

285.0 eV. The curves were fitted using Gaussian functions. Samples made from PbS CQDs were processed for cross-sectional TEM imaging. Zeiss NVision 40 focused ion beam (FIB) mill was used to prepare samples for TEM imaging. Thin films (approximately 100 nm) were prepared with a Ga⁺ beam followed by argon-ion nano milling. A FEI Titan 80–300 Cubed STEM was used for imaging.

Device Fabrication and Characterization. The PbS CQD film was deposited in a layer-by-layer fashion by spin-casting. PbS CQDs in octane (50 mg/mL) were dispensed on the substrate and spin-cast at 2500 rpm for 10 s for each layer. A 1% v/v 3-mercaptopropionic acid (MPA)/methanol solution was then dispensed to cover the entire substrate and spun after 3 s at the same speed for 5 s. Two rinses with methanol were applied for each layer. A top electrode consisting of 7.5 nm of MoO₃, 50 nm of Au, and 120 nm of Ag was deposited by thermal (MoO₃ and Ag) and electron beam (Au) evaporation at a pressure of $< 1 \times 10^{-6}$ Torr. The contact size defined by a shadow mask was 0.06 cm². Optical absorption measurements were carried out in a Cary 500 UV–vis–IR spectrophotometer using an integrating sphere.

J–V Characterization. AM 1.5 performance measurements were conducted using a class A (<25% spectral mismatch) solar simulator (ScienceTech). The bias sweep was performed using a Keithley 2400 digital multimeter. The source intensity was measured using a Melles–Griot broadband powermeter through a circular aperture of 0.049 cm² and set to be 100 mW cm². We used an aperture slightly smaller than the top electrode to avoid overestimating the photocurrent: the entire photon fluence passing through the aperture was counted as incident on the device for all analyses of J_{SC} and EQE.⁵⁰ The spectral mismatch of the system was characterized using a calibrated reference solar cell (Newport). The total AM1.5 spectral mismatch, taking into account the simulator spectrum and the spectral responsivities of the test cell, reference cell, and broadband power meter, was remeasured periodically and found to be $\sim 11\%$. This multiplicative factor, $M = 0.89$, was applied to the current density values of the J–V curve to most closely resemble true AM 1.5 performance.⁵¹ The test cell was mounted in a thermoelectric cooled holder with temperature feedback. The testing temperature was measured with a thermal couple and stabilized at 25.0 ± 0.1 °C according to the ISO standard. The total accuracy of the AM1.5 power conversion efficiency measurements was estimated to be $\pm 7\%$.

External Quantum Efficiency (EQE). EQE measurements were generated by a 400 W Xe (Horiba Jobin-Yvon) lamp. The light was passed through a monochromator (Horiba Jobin-Yvon FL-1039), filters (Newport) and an optical chopper operating at 100 Hz coupled to the input of a Stanford Research Systems lock-in amplifier. The collimated light output was measured through a 0.049 cm² aperture with calibrated Newport 818-UV and Newport 818-IR power meters. The photogenerated current was measured using a lock-in amplifier. The measurement step was 20 nm and the intensity varied with the spectrum of the Xe lamp.

Conflict of Interest: The authors declare no competing financial interest.

Acknowledgment. This publication is based in part on work supported by awards KUS-11-009-21 and GRP-CF-2011-21-P/S, made by King Abdullah University of Science and Technology (KAUST). V.M.B. acknowledges the support of the Oxford Martin School Fellowship and the Oxford Martin School.

A.G. acknowledges the support of the Wolfson/Royal Society Merit Award, a Reintegration Grant under EC Framework VII, and the support of the EPSRC through Grant No. EP/I017070/1. We acknowledge the work of E. Palmiano, R. Wolowiec, and D. Kopolovic. We acknowledge the Canada Foundation for Innovation, project number 19119, the Ontario Research Fund of the Centre for Spectroscopic Investigation of Complex Organic Molecules and Polymers, and the Natural Sciences and Engineering Research Council (NSERC) of Canada for funding.

Supporting Information Available: Growth-stage kinetics simulation details; XPS data for Pb and S elements comparing the PbS QCDs made from batch synthesis and dual-stage flow reactor synthesis. This material is available free of charge via the Internet at <http://pubs.acs.org>.

REFERENCES AND NOTES

- Talpin, D. V.; Lee, J. S.; Kovalenko, M. V.; Shevchenko, E. V. Prospects of Colloidal Nanocrystals for Electronic and Optoelectronic Applications. *Chem. Rev.* **2010**, *110*, 389–458.
- Sargent, E. H. Colloidal Quantum Dot Solar Cells. *Nat. Photonics* **2012**, *6*, 133–135.
- Mitzi, D. B.; Yuana, M.; Liua, W.; Kellock, A. J.; Cheya, S. J.; Gignac, L.; Schrott, A. G. Hydrazine-Based Deposition Route for Device-Quality CIGS Films. *Thin Solid Films* **2009**, *517*, 2158–2162.
- Guo, Q.; Ford, G. M.; Agrawal, R.; Hillhouse, H. W. Ink Formulation and Low-Temperature Incorporation of Sodium to Yield 12% Efficient Cu(In,Ga)(S,Se)₂ Solar Cells from Sulfide Nanocrystal Inks. *Prog. Photovolt: Res. Appl.* **2013**, *21*, 64–71.
- Guo, Q.; Ford, G. M.; Yang, W. C.; Walker, B. C.; Stach, E. A.; Hillhouse, H. W.; Agrawal, R. Fabrication of 7.2% Efficient CZTSSe Solar Cells Using CZTS Nanocrystals. *J. Am. Chem. Soc.* **2010**, *132* (49), 17384–17386.
- Ford, G. M.; Guo, Q.; Agrawal, R.; Hillhouse, H. W. Earth Abundant Element Cu₂Zn(Sn_{1-x}Ge_x)S₄ Nanocrystals for Tunable Band Gap Solar Cells: 6.8% Efficient Device Fabrication. *Chem. Mater.* **2011**, *23* (10), 2626–2629.
- Ip, A. H.; Thon, S. M.; Hoogland, S.; Voznyy, O.; Zhitomirsky, D.; Debnath, R.; Levina, L.; Rollny, L. R.; Carey, G. H.; Fischer, A.; et al. Hybrid Passivated Colloidal Quantum Dot Solids. *Nat. Nanotechnol.* **2012**, *7*, 577–582.
- Lan, X.; Bai, J.; Masala, S.; Thon, S. M.; Ren, Y.; Kramer, I. J.; Hoogland, S.; Simchi, A.; Koleilat, G. I.; Paz-Soldan, D.; et al. Self-Assembled, Nanowire Network Electrodes for Depleted Bulk Heterojunction Solar Cells. *Adv. Mater.* **2013**, *25*, 1769–1773.
- Ning, Z.; Zhitomirsky, D.; Adinolfi, V.; Sutherland, B.; Xu, J.; Voznyy, O.; Maraghechi, P.; Lan, X.; Hoogland, S.; Ren, Y.; et al. Graded Doping for Enhanced Colloidal Quantum Dot Photovoltaics. *Adv. Mater.* **2013**, *25*, 1719–1723.
- Moreels, I.; Justo, Y.; De, G. B.; Haustraete, K.; Martins, J. C.; Hens, Z. Size-Tunable, Bright, and Stable PbS Quantum Dots: a Surface Chemistry Study. *ACS Nano* **2011**, *5*, 2004–2012.
- Hines, M. A.; Scholes, G. D. Colloidal PbS Nanocrystals with Size-Tunable Near-Infrared Emission: Observation of Post-Synthesis Self-Narrowing of the Particle Size Distribution. *Adv. Mater.* **2003**, *15*, 1844–1849.
- Debnath, R.; Bakr, O.; Sargent, E. H. Solution-Processed Colloidal Quantum Dot Photovoltaics: a Perspective. *Energy Environ. Sci.* **2011**, *4*, 4870–4881.
- Yang, H.; Luan, W.; Tu, S. T.; Wang, Z. M. Synthesis Of Nanocrystals via Microreaction With Temperature Gradient: Towards Separation Of Nucleation And Growth. *Lab Chip* **2008**, *8*, 451–455.
- Yen, B. K. H.; Gunther, A.; Schmidt, M. A.; Jensen, K. F.; Bawendi, M. G. A Microfabricated Gas-Liquid Segmented Flow Reactor for High-Temperature Synthesis: the Case of CdSe Quantum Dots. *Angew. Chem., Int. Ed.* **2005**, *44*, 5447–5451.
- Yen, B. K. H.; Stott, N. E.; Jensen, K. F.; Bawendi, M. G. A Continuous-Flow Microcapillary Reactor for the Preparation of a Size Series Of CdSe Nanocrystals. *Adv. Mater.* **2003**, *15*, 1858–1862.
- Marre, S.; Jensen, K. F. Synthesis Of Micro and Nanostructures in Microfluidic Systems. *Chem. Soc. Rev.* **2010**, *39*, 1183–1202.
- Edel, J. B.; Fortt, R.; de Mello, J. C.; de Mello, A. J. Microfluidic Routes to the Controlled Production of Nanoparticles. *Chem. Commun.* **2002**, 1136–1137.
- Nightingale, A. M.; de Mello, J. C. Segmented Flow Reactors for Nanocrystal Synthesis. *Adv. Mater.* **2012**, *25*, 1813–1821.
- Jahn, A.; Reiner, J. E.; Vreeland, W. N.; DeVoe, D. L.; Locascio, L. E.; Gaitan, M. Preparation of Nanoparticles by Continuous-Flow Microfluidics. *J. Nanopart. Res.* **2008**, *10*, 925–934.
- Boleininger, J.; Kurz, A.; Reuss, V.; Soennichsen, C. Microfluidic Continuous Flow Synthesis of Rod-Shaped Gold and Silver Nanocrystals. *Phys. Chem. Chem. Phys.* **2006**, *8*, 3824–3827.
- Wagner, J.; Koehler, J. M. Continuous Synthesis of Gold Nanoparticles in a Microreactor. *Nano Lett.* **2005**, *5*, 685–691.
- Song, Y.; Modrow, H.; Henry, L. L.; Saw, C. K.; Doomes, E. E.; Palshin, V.; Holmes, J.; Kumar, C. S. S. R. Microfluidic Synthesis of Cobalt Nanoparticles. *Chem. Mater.* **2006**, *18*, 2817–2827.
- Song, Y.; Kumar, C. S. S. R.; Holmes, J. Synthesis of Palladium Nanoparticles Using a Continuous Flow Polymeric Microreactor. *J. Nanosci. Nanotechnol.* **2004**, *4*, 788–793.
- Song, Y.; Doomes, E. E.; Prindle, J.; Tittsworth, R.; Holmes, J.; Kumar, C. S. S. R. Investigations into Sulfobetaine-Stabilized Cu Nanoparticle Formation: Toward Development of a Microfluidic Synthesis. *J. Phys. Chem. B* **2005**, *109*, 9330–9338.
- Mehenni, H.; Sinatra, L.; Mahfouz, R.; Katsiev, K.; Bakr, O. M. Rapid Continuous Flow Synthesis of High-Quality Silver Nanocubes and Nanospheres. *RSC Adv.* **2013**, *10.1039/c3ra43295e*.
- Wacker, J. B.; Lignos, I.; Parashar, V. K.; Gijis, M. A. M. Controlled Synthesis of Fluorescent Silica Nanoparticles Inside Microfluidic Droplets. *Lab Chip* **2012**, *12*, 3111–3116.
- Khan, S. A.; Guenther, A.; Schmidt, M. A.; Jensen, K. F. Microfluidic Synthesis of Colloidal Silica. *Langmuir* **2004**, *20*, 8604–8611.
- Cottam, B. F.; Krishnadasan, S.; de Mello, A. J.; de Mello, J. C.; Shaffer, M. S. P. Accelerated Synthesis of Titanium Oxide Nanostructures Using Microfluidic Chips. *Lab Chip* **2007**, *7*, 167–169.
- Abou-Hassan, A.; Sandre, O.; Neveu, S.; Cabuil, V. Synthesis of Goethite by Separation of the Nucleation and Growth Processes of Ferrihydrite Nanoparticles Using Microfluidics. *Angew. Chem., Int. Ed.* **2009**, *48*, 2342–2345.
- Lee, W.-B.; Weng, C.-H.; Cheng, F.-Y.; Yeh, C.-S.; Lei, H.-Y.; Lee, G.-B. Biomedical Microdevices Synthesis of Iron Oxide Nanoparticles Using a Microfluidic System. *Biomed. Microdevices* **2009**, *11*, 161–171.
- Abou-Hassan, A.; Neveu, S.; Dupuis, V.; Cabuil, V. Synthesis of Cobalt Ferrite Nanoparticles in Continuous-Flow Microreactors. *RSC Adv.* **2012**, *2*, 11263–11266.
- Hassan, N.; Cabuil, V.; Abou-Hassan, A. Continuous Multi-step Microfluidic Assisted Assembly of Fluorescent, Plasmonic, and Magnetic Nanostructures. *Angew. Chem., Int. Ed.* **2013**, *52*, 1841.
- Abdelhady, A. L.; Afzaal, M.; Malik, M. A.; O'Brien, P. Flow Reactor Synthesis of CdSe, CdS, CdSe/CdS and CdSeS Nanoparticles from Single Molecular Precursor(s). *J. Mater. Chem.* **2011**, *21*, 18768–18775.
- Shestopalov, I.; Tice, J. D.; Ismagilov, R. F. Multi-Step Synthesis of Nanoparticles Performed on Millisecond Time Scale in a Microfluidic Droplet-Based System. *Lab Chip* **2004**, *4*, 316–321.
- Chan, E. M.; Alivisatos, A. P.; Mathies, R. A. High-Temperature Microfluidic Synthesis of CdSe Nanocrystals in Nanoliter Droplets. *J. Am. Chem. Soc.* **2005**, *127*, 13854–13861.

36. Krishnadasan, S.; Tovilla, J.; Vilar, R.; deMello, A. J.; deMello, J. C. On-Line Analysis of CdSe Nanoparticle Formation in a Continuous Flow Chip-Based Microreactor. *J. Mater. Chem.* **2004**, *14*, 2655–2660.
37. Chan, E. M.; Mathies, R. A.; Alivisatos, A. P. Size-Controlled Growth of CdSe Nanocrystals in Microfluidic Reactors. *Nano Lett.* **2003**, *3*, 199–201.
38. Nightingale, A. M.; de Mello, J. C. Controlled Synthesis of III–V Quantum Dots in Microfluidic Reactors. *Chem-PhysChem* **2009**, *10*, 2612–2614.
39. Jin, H.-D.; Chang, C.-H. Continuous Synthesis of SnTe Nanorods. *J. Mater. Chem.* **2011**, *21*, 12218–12220.
40. Nightingale, A. M.; de Mello, J. C. Microscale Synthesis of Quantum Dots. *J. Mater. Chem.* **2010**, *20*, 8454–8463.
41. Lifshitz, I. M.; Slyozov, V. V. On Kinetics of Diffusion Decay of Oversaturated Solid Solutions. *J. Exp. Theor. Phys.* **1958**, *35*, 479–492.
42. Lifshitz, I. M.; Slyozov, V. V. Kinetics of Diffusive Decomposition of Supersaturated Solid Solutions. *Sov. Phys. JETP* **1959**, *8*, 331–339.
43. Lifshitz, I. M.; Slyozov, V. V. The Kinetics of Precipitation from Supersaturated Solid. *J. Phys. Chem. Solids* **1961**, *19*, 35–50.
44. Smith, N. A. S.; Burlakov, V. M.; Ramos, Á. M. Mathematical Modeling of the Growth and Coarsening of Ice Particles in the Context of High Pressure Shift Freezing Processes. *J. Phys. Chem. B* **2013**, *117*, 8887–8895.
45. Burlakov, V. M.; Kantorovich, L. Ostwald Ripening of Binary Alloy Particles. *J. Chem. Phys.* **2011**, *134*, 024521.
46. Rempel, J. Y.; Bawendi, M. G.; Jensen, K. F. Insights into The Kinetics of Semiconductor Nanocrystal Nucleation and Growth. *J. Am. Chem. Soc.* **2009**, *131*, 4479–4489.
47. van Embden, J.; Sader, J. E.; Davidson, M.; Mulvaney, P. Evolution of Colloidal Nanocrystals: Theory and Modeling of their Nucleation and Growth. *J. Phys. Chem. C* **2009**, *113*, 16342–16355.
48. Pattantyus-Abraham, A. G.; Kramer, I. J.; Barkhouse, A. R.; Wang, X. H.; Konstantatos, G.; Debnath, R.; Levina, L.; Raabe, I.; Nazeeruddin, M. K.; Gratzel, M.; et al. Depleted-Heterojunction Colloidal Quantum Dot Solar Cells. *ACS Nano* **2010**, *4*, 3374–3380.
49. 3M Manufacturing and Industry: Fluorinert FC-70 Product Information. **2000**, 98-0212-2307-2 (HB).
50. Snaith, H. J. The Perils of Solar Cell Efficiency Measurements. *Nat. Photon.* **2012**, *6*, 337–340.
51. Kroon, J. M.; Wienk, M. M.; Verhees, W. J. H.; Hummelen, J. C. Accurate Efficiency Determination and Stability Studies of Conjugated Polymer/Fullerene Solar Cells. *Thin Solid Films* **2002**, *223*, 403–404.